

Coupled-wire construction of non-Abelian higher-order topological phases

Jiaxin Pan¹ and Longwen Zhou^{1,2,3,*}

¹*College of Physics and Optoelectronic Engineering,
Ocean University of China, Qingdao, China 266100*

²*Key Laboratory of Optics and Optoelectronics, Qingdao, China 266100*

³*Engineering Research Center of Advanced Marine Physical Instruments and Equipment of MOE, Qingdao, China 266100*

(Dated: 2025-12-25)

Non-Abelian topological charges (NATCs), characterized by their noncommutative algebra, offer a framework for describing multigap topological phases beyond conventional Abelian invariants. While higher-order topological phases (HOTPs) host boundary states at corners or hinges, their characterization has largely relied on Abelian invariants such as winding and Chern numbers. Here, we propose a coupled-wire scheme of constructing non-Abelian HOTPs and analyze a non-Abelian second-order topological insulator as its minimal model. The resulting Hamiltonian supports hybridized corner modes, protected by parity-time-reversal plus sublattice symmetries and described by a topological vector that unites a non-Abelian quaternion charge with an Abelian winding number. Corner states emerge only when both invariants are nontrivial, whereas weak topological edge states of non-Abelian origins arise when the quaternion charge is nontrivial, enriching the bulk-edge-corner correspondence. The system further exhibits both non-Abelian and Abelian topological phase transitions, providing a unified platform that bridges these two distinct topological classes. Our work extends the understanding of HOTPs into non-Abelian regimes and suggests feasible experimental realizations in synthetic quantum systems, such as photonic or acoustic metamaterials.

I. INTRODUCTION

Topological matter has emerged as an active research area in quantum and condensed matter physics over the past decades [1–7]. Principally, a topological phase is characterized by global order parameters, protected by spatial and internal symmetries, holds degenerate edge states associated to its bulk topology, and showing topologically quantized responses to external perturbations. Moreover, a topological transition between distinct phases of the same symmetry class does not accompany any symmetry breaking, making it to go beyond the traditional Landau-Ginzburg-Wilson paradigm of phase transitions [8]. From the discovery of integer quantum Hall effects [9, 10] to the theoretical and experimental progress on quantum anomalous Hall effects [11–13] and quantum spin Hall effects [14–17], a general framework for understanding topological phases of matter is gradually established, which has profoundly reshaped our understanding of quantum matter and spurred continued research on topological materials [18–20]. More recently, the exploration of topological phenomena has been extended to non-Hermitian [21–25] and periodically driven (Floquet) setups [26–30], further extending the scope of the field to nonequilibrium and open systems. Building on these foundations, the classification of topological matter has been formulated within the Altland-Zirnbauer symmetry class. This so-called “tenfold way” provides a unified framework for characterizing all possible topological phases of free fermions in different spatial dimensions according to their time-reversal, particle-hole, and chiral

symmetries [31], laying the groundwork for later extensions to non-Hermitian [32–34] and driven systems [35–37]. Typically, the topological phases considered in these studies are described by \mathbb{Z} or \mathbb{Z}_2 invariants, such as Chern and winding numbers. As these invariants are commutative and belong to Abelian groups, they could be regarded as Abelian topological charges.

On the other hand, the concept of non-Abelian topological charge (NATC) has attracted increasing attention over the years. It provides a unified framework for describing noncommutative topological structures in systems with multiple bands/gaps and possessing \mathcal{PT} or $\mathcal{C}_2\mathcal{T}$ symmetry. NATC was originally utilized to characterize the biaxial nematic liquid crystal [38–40], and recently been incorporated into the study of emerging topological semimetals and insulators [41–64] that fall outside the tenfold way of conventional symmetry classifications. In non-Abelian topological semimetals, the NATC is used to characterize the knot and braiding structures of nodal lines or nodal points in different band gaps [41]. Such distributed multigap degeneracies lead to complex topological configurations that cannot be captured by standard approaches based on Abelian geometric phases. In two-dimensional (2D) three-band systems, such gapless degeneracies can be characterized by the Euler class [42], whose non-Abelian topology has been experimentally observed [43–47]. In non-Abelian topological insulators (NATIs), the NATC can be used to distinguish different topological phases that correspond to distinct configurations of edge states located in different band gaps. This framework overcomes the limitations of Abelian geometric phases, such as the Zak or Berry phases, which could not identify all possible topological states and establish their bulk-edge correspondence. In particular, even when the underlying Bloch states of

* zhoulw13@u.nus.edu

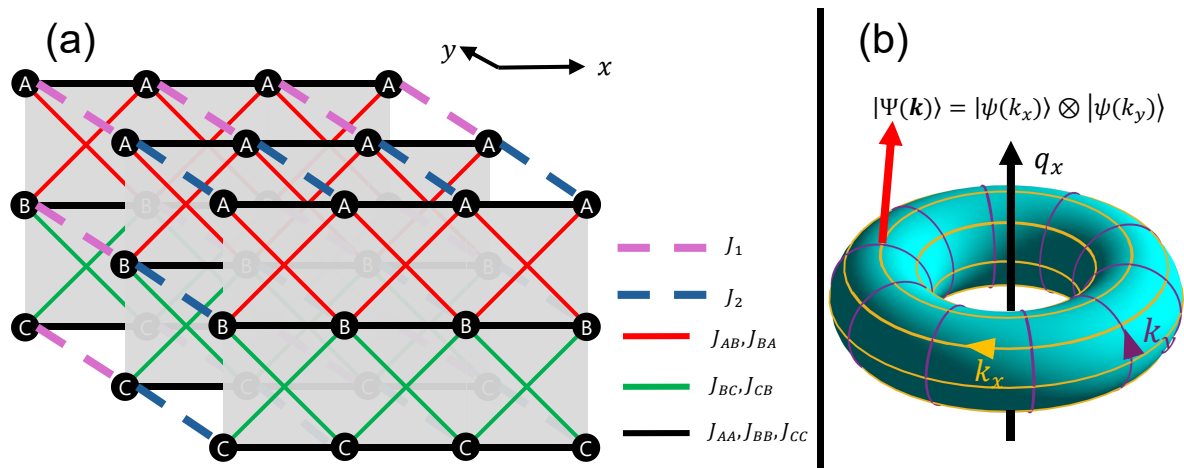


FIG. 1. Illustration of the 2D lattice model and its Brillouin zone. (a) shows the model realized by stacking 1D trimer chains. Along x direction, each unit cell has three sublattices with onsite potentials S_A, S_B, S_C . Couplings between neighboring sites are indicated by red and green lines, corresponding to $J_{AB(BA)}$ and $J_{BC(CB)}$, respectively, where we take $J_{AB} = J_{BA} = iu$ and $J_{BC} = J_{CB} = iv$. Couplings between the same kind of sublattices are shown as black bonds, representing J_{AA}, J_{BB} and J_{CC} . Along y direction, coupling strengths alternate between J_1 and J_2 in purple and blue dashed lines. (b) shows the 2D Brillouin zone on a torus.

the system are all real vectors and the resulting Zak phase is trivial, topological edge states of non-Abelian origins may still emerge under the open-boundary condition (OBC). Non-Abelian topological phases thus go beyond the conventional understanding of topological insulators or superconductors. Following rapid theoretical developments, experimental progress has also been made in realizing non-Abelian topological phases in quantum and quantum-inspired simulators, including transmission line networks [50, 51], photonics [52, 53, 63], acoustic metamaterials [54, 55, 62], and ultracold atoms [56].

In the past decade, a unique class of topological phases was revealed, in which topological boundary states can emerge on “higher-order surfaces” (such as the corners or hinges of a cubic material) of the system. They are thus referred to as HOTPs. More precisely, and as a hallmark feature of HOTPs, a d -dimensional, n th-order topological phase ($1 < n \leq d$) has symmetry-protected boundary states of dimensions $d - n$ [65–74]. In the early development of this concept, the topological quadrupole insulator plays a key role, demonstrating the very existence of HOTPs and providing a rigorous theoretical foundation for their description [65]. Typically, HOTPs require crystalline symmetries [65–69], such as rotation, mirror inversion, and other spatial symmetries for their protections. Meanwhile, a correspondence was established between the existence of zero-dimensional corner states and the winding numbers of one-dimensional (1D) edges in sublattice-symmetric higher-order topological insulators (HOTIs) [70], making it possible to realize HOTPs even without crystalline symmetries [70–73]. Until now, HOTPs have been realized in different experimental settings [75–77] and also considered very recently in non-Abelian regimes [58–60].

In this work, we introduce a unique class of non-

Abelian HOTPs, which are obtainable via staggered couplings of 1D non-Abelian topological chains along extra dimensions. Focusing on a 2D lattice model with hybridized non-Abelian and Abelian topology as illustrations, we reveal a rich set of non-Abelian second-order topological insulators (SOTIs) with degenerate corner states, which are protected by intrinsic \mathcal{PT} and chiral symmetries. The resulting phase diagram of the system shows multiple phases and transitions, with each of them being characterized by a hybridized topological charge carrying a quaternion and an integer as its components. Further connections are established among these hybridized changes, topological corner states, and 1D non-Abelian edge bands, offering a unified perspective on the bulk-edge-corner correspondence. Our results thus extend the study of HOTPs to non-Abelian regimes and establish a connection between non-Abelian and Abelian topological matter in a single setup. The rest of the paper is organized as follows. In Sec. II, we introduce our theory, sketch the general idea for its implementation, and construct our 2D model of non-Abelian SOTIs [see Fig. 1(a) for an illustration of its lattice geometry]. In Sec. III, hybridized non-Abelian topological charges are defined to characterize both the non-Abelian and Abelian topology of our system on an equal footing, leading to its bulk topological phase diagram. In Sec. IV, we study topological boundary states of our system under OBC and reveal its bulk-edge-corner correspondence of non-Abelian origins. The found topological phases host not only corner states but also weak non-Abelian edge bands, with both of them being captured by the hybridized charge we introduced. In Sec. V, we summarize our results and discuss experimental prospects. Further theoretical and numerical details are given in the Appendices A and B.

II. THEORY AND MODEL

In this section, we first introduce a theoretical framework to construct HOTPs of non-Abelian characters. The general idea is to couple non-Abelian and/or Abelian topological lattices along different spatial dimensions, yielding a higher-dimensional system whose HOTPs are determined by the product topology of its lower-dimensional subsystems, as detailed in Sec. II A. The non-Abelian HOTPs thus obtained are referred to as pristine (hybridized) if none (some) of its constituting subsystems are characterized by Abelian topological charges. The minimal case following such a construction is given by hybridized non-Abelian SOTIs in two dimensions, whose lattice Hamiltonian is introduced and analyzed in Sec. II B. More thorough treatments of the topology and phase transitions in our model are given in later sections.

A. Theory

In previous work, the coupled-wire construction has been successfully used to realize Abelian HOTPs in both static and driven systems [73, 78–81]. Here, we generalize the existing scheme for building a unique class of non-Abelian HOTPs. We start with a set of Hamiltonians $\{H_{x_n} | n = 1, 2, \dots, d-1, d\}$, where each H_{x_n} describes a 1D chain of free fermions along a separate spatial dimension. Taking Kronecker sum among different H_{x_n} , we obtain the lattice Hamiltonian of a d -dimensional system, i.e.,

$$H = H_{x_1} \oplus H_{x_2} \oplus \dots \oplus H_{x_{d-1}} \oplus H_{x_d}. \quad (1)$$

Here, $A \oplus B = A \otimes \mathbb{I}_B + \mathbb{I}_A \otimes B$ for any operators A and B , with \mathbb{I}_A and \mathbb{I}_B be identities of the Hilbert spaces of A and B . The system described by H could possess emergent HOTPs due to the interplay of lower-dimensional topological states among its subsystems H_{x_n} . For example, if each H_{x_n} describes a topological insulator with a topologically nontrivial edge state $|\psi_{x_n}\rangle$ of energy E_{x_n} , i.e., $H_{x_n}|\psi_{x_n}\rangle = E_{x_n}|\psi_{x_n}\rangle$ for $n = 1, \dots, d$, the composite system H must have a localized topological state $|\psi\rangle = |\psi_{x_1}\rangle \otimes |\psi_{x_2}\rangle \otimes \dots \otimes |\psi_{x_{d-1}}\rangle \otimes |\psi_{x_d}\rangle$ of energy $E = \sum_{n=1}^d E_{x_n}$ at one of its zero-dimensional corners. The resulting d -dimensional, d th-order topological phase is characterized by a Cartesian-product invariant $\nu = (w_1, w_2, \dots, w_{d-1}, w_d)$, with w_n be the topological number classifying the phases of 1D subsystem H_{x_n} . It is clear that the corner state $|\psi\rangle$ could appear if and only if all components of ν are nontrivial, so that every $|\psi_{x_n}\rangle$ exists as a topological edge state of H_{x_n} , confirming the higher-order topology of the system described by H .

The aforementioned scheme can be used to generate non-Abelian HOTPs by letting at least one out of the set $\{H_{x_n} | n = 1, 2, \dots, d-1, d\}$ of subsystems to hold 1D non-Abelian topological states. The resulting non-Abelian HOTPs can be further organized into two subclasses. The first subclass, in which the subsystem H_{x_n} is char-

acterized by a non-Abelian topological charge Q_{x_n} for every $n = 1, \dots, d$, is referred to as pristine non-Abelian HOTPs. For example, let us consider a system described by Hamiltonian $H = H_x \oplus H_y$, with both H_x and H_y depicting 1D, three-band models of non-Abelian topological insulators characterized by quaternion charges $Q_x \in \mathbb{Q}_8$ and $Q_y \in \mathbb{Q}_8$ in the quaternion group \mathbb{Q}_8 . The 2D system H could then support pristine non-Abelian SOTIs, with each of them being characterized by a non-Abelian topological charge $\nu = (Q_x, Q_y) \in \mathbb{Q}_8 \times \mathbb{Q}_8$ and possessing localized eigenmodes at lattice corners if both Q_x and Q_y are different from the unit element of \mathbb{Q}_8 . The second subclass, in which a finite set of subsystems (e.g., $\{H_{x_n} | n = 1, \dots, l; l < d\}$) allow only Abelian topological phases, is referred to as hybridized non-Abelian HOTPs. For example, let us still consider a system described by $H = H_x \oplus H_y$, with H_x (H_y) depicting a 1D, three-band (two-band) model of non-Abelian (Abelian) topological insulators characterized by quaternion charge $Q_x \in \mathbb{Q}_8$ (winding number $w_y \in \mathbb{Z}$). The 2D system H would now support hybridized non-Abelian SOTIs, with each of them being depicted by a topological charge $\nu = (Q_x, w_y) \in \mathbb{Q}_8 \times \mathbb{Z}$ and possessing corners-localized eigenstates if Q_x is not the unit element and $w_y \neq 0$.

Before proceeding to explicit examples, let us analyze a few more cases. Focusing on three dimensions, there could be three types of non-Abelian third-order topological phases with localized corner states and three types of non-Abelian second-order topological phases with chiral hinge states according to our scheme. The non-Abelian third-order topological phases, having the common Hamiltonian $H = H_x \oplus H_y \oplus H_z$, are pristine (hybridized) ones if all (one or two) of the subsystems are characterized by non-Abelian (Abelian) topological charges. The non-Abelian second-order topological phases have the common Hamiltonian $H = H_{xy} \oplus H_z$, where H_{xy} (H_z) represents a 2D (1D) subsystem. When both the H_{xy} and H_z are characterized by non-Abelian topological charges, the system H would support pristine non-Abelian edge states along its hinges at the xy -surfaces with $z = 0$ and $z = L_z$ for a cubic lattice. Similar configurations of hinge states appear when the H_{xy} and H_z describe non-Abelian and Abelian topological insulators, respectively, with the key difference that the resulting second-order topological phases are hybridized. If the H_{xy} and H_z separately describe an Abelian Chern insulator and a non-Abelian topological insulator, the system H would support hybridized non-Abelian SOTIs with chiral hinge modes lying along the boundaries of their xy -surfaces with $z = 0$ and $z = L_z$ for a cubic lattice.

In principle, one can carry forward this procedure to acquire d -dimensional, n th-order non-Abelian HOTPs, either pristine or hybridized, with $(d - n)$ -dimensional boundary modes for any $1 < n \leq d$. In the rest of this study, we focus on the minimal case of non-Abelian HOTPs characterized by the hybridized topological charge $\nu = (Q_x, w) \in \mathbb{Q}_8 \times \mathbb{Z}$ in two dimensions. Its simplest construction is illustrated in Fig. 1.

We note that non-Abelian HOTPs may also be realized by exploiting the geometric nature of NATC. For a 1D system, the Hamiltonian in momentum space can be written as $H(k_x) = R(k_x)\Lambda R^\top(k_x)$, where Λ is the eigenvalue matrix and $R(k_x)$ contains eigenvectors. A 2D version can be made by considering a Hamiltonian $H(k_x, k_y) = R_2(k_y)R_1(k_x)\Lambda R_1^\top(k_x)R_2^\top(k_y)$, which extends the non-Abelian structures of eigenvectors in $R_1(k_x)$ and $R_2(k_y)$ to two dimensions [58]. This construction allows the non-Abelian topology along two momentum directions k_x and k_y to be characterized independently. One may associate a NATC Q_x with the eigenframe rotation of $R_1(k_x)$ vs k_x and another NATC Q_y with the rotation of $R_2(k_y)$ along k_y . The global NATC can be given by $q = (Q_x, Q_y)$, which cannot appear in arbitrary combinations in a gapped system. To see this, let us initialize the 2D state at $(k_x, k_y) = (-\pi, -\pi)$. If this state is first transported along k_x and then along k_y across the Brillouin zone to reach (π, π) , the resulting rotation matrix is $Q_y Q_x$. Instead, if the evolution is performed first along k_y and then k_x , the resulting matrix reads $Q_x Q_y$. These two paths, although connecting the same initial and final points, lead to different results if $[Q_x, Q_y] \neq 0$. But this could only happen when the energy bands exhibit degeneracies. If the chosen path in k -space crosses such a degeneracy, the NATC may change abruptly, allowing noncommuting charges to appear simultaneously. Following this scheme, non-Abelian corner states can emerge in 2D four-band systems characterized by two independent group elements in the generalized quaternion group \mathbb{Q}_{16} . For systems depicted by the quaternion group Q_8 , only two distinct types of edge state can appear [58].

B. Model

We now propose a minimal model of non-Abelian HOTPs by stacking 1D trimer chains along a second dimension, where the interchain coupling strengths alternate along the stacking direction as illustrated in Fig. 1(a). The Hamiltonian of the resulting 2D lattice model reads

$$\begin{aligned}
H = & \sum_{n,m=1}^{N,M/2} \sum_{\alpha,\beta=A,B,C} [(J_1 |n, 2m, \alpha\rangle \langle n, 2m-1, \alpha| \\
& + J_2 |n, 2m+1, \alpha\rangle \langle n, 2m, \alpha| + \text{h.c.}) \\
& + S_\alpha |n, m, \alpha\rangle \langle n, m, \alpha| \\
& + (J_{\alpha\beta} |n+1, m, \beta\rangle \langle n, m, \alpha| + \text{h.c.})],
\end{aligned} \tag{2}$$

where n and m denote unit cell and lattice indices along x and y directions. N ($M/2$) denotes the number of unit cells along x (y). α and β label sublattice degrees of freedom along x . The terms $J_{\alpha\beta}$ represent nearest-neighbor hopping amplitudes along x , with the constraint that $J_{AC} = J_{CA} = 0$. Explicitly, we set $J_{AB} = J_{BA} = iu$, and $J_{BC} = J_{CB} = iv$. S_α denotes the strength of onsite potential in sublattice α . J_1 and J_2 are nearest-neighbor

hopping amplitudes along y -direction. The Hilbert space of the 2D system is $3N \times M$ -dimensional. The Hamiltonian in Eq. (2) has the Kronecker sum structure of Eq. (1), which allows us to express it as

$$H = H_x \oplus H_y = H_x \otimes \mathbb{I}_y + \mathbb{I}_x \otimes H_y. \tag{3}$$

Here, the H_x and H_y represent 1D subsystems along x and y directions. They are explicitly given by

$$\begin{aligned}
H_x = & \sum_{n=1}^N \sum_{\alpha,\beta=A,B,C} [S_\alpha |n, \alpha\rangle \langle n, \alpha| \\
& + (J_{\alpha\beta} |n+1, \beta\rangle \langle n, \alpha| + \text{h.c.})], \\
H_y = & \sum_{m=1}^{M/2} (J_1 |2m\rangle \langle 2m-1| \\
& + J_2 |2m+1\rangle \langle 2m| + \text{h.c.}).
\end{aligned} \tag{4}$$

The eigenvalue equation of the 2D Hamiltonian H is given by $H|\Psi_q\rangle = E_q|\Psi_q\rangle$, where E_q is the energy of its q th eigenstate $|\Psi_q\rangle$. For the decoupled 1D Hamiltonian $H_{x(y)}$, the eigenvalue equation reads $H_{x(y)}|\Psi_{x(y)}\rangle = E_{x(y)}|\Psi_{x(y)}\rangle$. The spectrum of each 1D Hamiltonian is illustrated in Sec. III B. The Kronecker sum structure in Eq. (3) implies that for any eigenstate $|\Psi_q\rangle$ of H with energy E_q , there must be eigenstates $|\Psi_x\rangle$ and $|\Psi_y\rangle$ of the subsystems H_x and H_y with energies E_x and E_y , such that $|\Psi_q\rangle = |\Psi_x\rangle \otimes |\Psi_y\rangle$ and $E_q = E_x + E_y$. One could then deduce the eigensystem of H from the eigenstates and eigenenergies of its 1D subsystems H_x and H_y . This further allows our 2D system to inherit the topology of its lower dimensional components via hybridizing their non-Abelian and Abelian topological characters.

Under the OBC, if the H_x has an edge state $|\Psi_{xe}\rangle$ with energy E_{xe} , and the H_y has an edge state $|\Psi_{ye}\rangle$ with energy E_{ye} , the 2D Hamiltonian H in Eq. (2) would necessarily host a corner-localized state $|\Psi_c\rangle = |\Psi_{xe}\rangle \otimes |\Psi_{ye}\rangle$ with energy $E_c = E_{xe} + E_{ye}$. In our case, the Hamiltonian H_y along y -direction is just the well-known Su-Schrieffer-Heeger (SSH) model, which within its topological phase hosts two degenerate edge zero modes protected by chiral symmetry. Therefore, we have $E_{ye} = 0$ and the energy of corner states is $E_c = E_{xe}$, relying only on the edge state of H_x . Moreover, the number and degeneracy of corner states are primarily determined by the edge spectrum of H_x , as the SSH Hamiltonian H_y contributes only a fixed two-fold degeneracy for each corner state. For example:

- 1) If H_y has one pair of degenerate edge states, the 2D system H will exhibit four degenerate corner states.
- 2) If H_y has two such pairs at different energies, the 2D system H will have two sets of fourfold degenerate corner states.
- 3) If H_y has four edge modes at the same energy, the corner states of H will be eightfold degenerate.

More detailed evidence and numerical results are presented in the next two sections.

III. TOPOLOGICAL INVARIANTS AND PHASE DIAGRAM

This section first introduces the topological characterization for each of our 1D subsystems that constituting the 2D lattice model H . We obtain the topological invariants, edge states and bulk-edge correspondence for both the H_x and H_y . Building on these, we define the hybridized topological invariants for our 2D model and obtain its phase diagram, which shows a rich set of non-Abelian HOTPs.

A. Topological invariants of 1D subsystems

The direct sum structure of Hamiltonian H permits a natural definition of its subsystem topological invariants, thereby offering a link between the first and second order topology. Under periodic boundary condition (PBC), the Bloch Hamiltonians of H_x and H_y are given by

$$H_x(k_x) = \begin{pmatrix} V_{AA} & 2u \sin k_x & 0 \\ 2u \sin k_x & V_{BB} & 2v \sin k_x \\ 0 & 2v \sin k_x & V_{CC} \end{pmatrix}, \quad (6)$$

$$H_y(k_y) = (J_1 + J_2 \cos k_y)\sigma_1 + J_2 \sin k_y \sigma_2 \\ = d_1(k_y)\sigma_1 + d_2(k_y)\sigma_2. \quad (7)$$

Here, $V_{\alpha\alpha} \equiv S_\alpha + 2J_{\alpha\alpha} \cos k_x$ for $\alpha = A, B, C$. $\sigma_{1,2,3}$ and the x, y, z components of Pauli matrices. Along y direction, we have $H_y(k_y) |\psi_\pm(k_y)\rangle = E_\pm |\psi_\pm(k_y)\rangle$, where $E_\pm = \pm E_y$ due to chiral symmetry. Along x direction, we have $H_x(k_x) |\psi_p(k_x)\rangle = E_p |\psi_p(k_x)\rangle$, where $p = 1, 2, 3$. The states $|\psi_p(k_x)\rangle$ and $|\psi_\pm(k_y)\rangle$ are defined in two Hilbert subspaces \mathcal{H}_{k_x} and \mathcal{H}_{k_y} , respectively. They have distinct geometric and topological structures within their respective parameter manifolds \mathcal{M}_x and \mathcal{M}_y . The fundamental homotopy group of them can be expressed as $\pi_1(\mathcal{M}_x) = \mathbb{Z}$ and $\pi_1(\mathcal{M}_y) = \mathbb{Q}_8$ [50]. The 2D Bloch Hamiltonian reads

$$H(\mathbf{k}) = H_x(k_x) \otimes \sigma_0 + \mathbb{I}_3 \otimes H_y(k_y), \quad (8)$$

where σ_0 and \mathbb{I}_3 denote 2×2 and 3×3 identity matrices. As a result, the 2D model has six bulk bands, whose eigenenergies are $\pm E_{py} = E_p \pm E_y$ for $p = 1, 2, 3$ and the related eigenstates $|\Psi_{p\pm}(\mathbf{k})\rangle = |\psi_p(k_x)\rangle \otimes |\psi_\pm(k_y)\rangle$. The corresponding parameter space forms the Cartesian product $\mathcal{M} = \mathcal{M}_x \times \mathcal{M}_y$, with each point $\mathbf{k} \in \mathcal{M}$ associated with a quantum state $|\Psi_{p\pm}(\mathbf{k})\rangle$. This construction naturally defines a composite manifold structure in which the local state is induced by the tensor product of two fiber bundles, providing a geometric framework for describing coupled and multi-layer topological systems. In Fig. 1(b), we present the 2D Brillouin zone (BZ) of $H(\mathbf{k})$ on a torus with $k_x, k_y \in [-\pi, \pi]$. Each point \mathbf{k} on the surface spans six eigenenergies and eigenstates. Taking advantage of the tensor-product structure of $|\Psi_{p\pm}(\mathbf{k})\rangle$, we can study the contribution of the two subsystem Hamil-

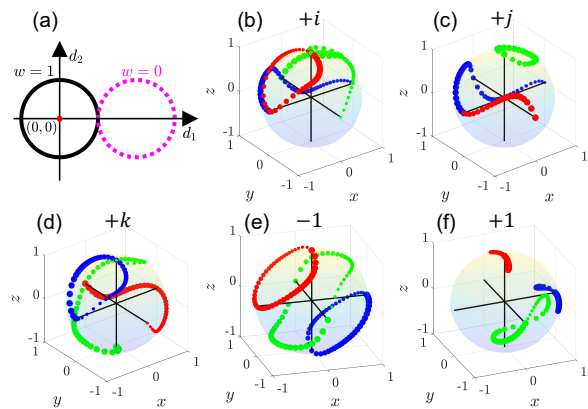


FIG. 2. Geometric illustrations of the Abelian winding number and non-Abelian quaternion charge. (a) shows the trajectory of Bloch vector $\mathbf{d}(k_y)$ as k_y varies from $-\pi$ to π . In the topological (trivial) phase with winding number $w = 1$ ($w = 0$), the trajectory of $\mathbf{d}(k_y)$ in black solid line (pink dashed line) encircles once (does not encircle) the origin. (b)-(f) show the eigenframe rotation associated with each quaternion charge. The eigenstates $|\psi_{1,2,3}(k_x)\rangle$ are marked by red, green, and blue dots at every k_x . The size of dots in each group increases progressively from $k_x = -\pi$ to π .

tonians $H_x(k_x)$ and $H_y(k_y)$ to the topological properties of the 2D lattice model separately.

Along the meridional direction of the tours, we connect the ends of BZ along the y direction, such that the quasimomentum k_y forms a closed loop for each k_x , as illustrated by the purple loop in Fig. 1(b). The eigenstates $\{|\psi(k_x)\rangle\}$ are independent of k_y , so that only $|\psi(k_y)\rangle$ contributes to the topological invariant along this loop. According to the construction of our 2D system, the Hamiltonian H_y takes the form of an SSH model, which belongs to the BDI symmetry class [3]. The topological properties of H_y can be characterized by a winding number due to its chiral symmetry $\Gamma = \sigma_3$, i.e.,

$$w = \frac{1}{2\pi} \int_{-\pi}^{\pi} \frac{d_1(k_y)\partial_{k_y} d_2(k_y) - d_2(k_y)\partial_{k_y} d_1(k_y)}{|\mathbf{d}(k_y)|^2} dk_y, \quad (9)$$

where $\mathbf{d}(k_y) = (d_1(k_y), d_2(k_y))$. The w has a geometric interpretation: it counts the number of times the Bloch vector $\mathbf{d}(k_y)$ winds around the origin of d_1 - d_2 plane as k_y varies from $-\pi$ to π , as illustrated in Fig. 2(a). There are two distinct phases for $H_y(k_y)$. In the topological insulator phase with $w = 1$ (black line), the Hamiltonian H_y hosts two zero-energy edge states under OBC [Fig. 3(a)]. In the trivial insulator phase with $w = 0$ (magenta dashed line), no edge states appear. At the phase transition ($d_1 = d_2 = 0$), the origin lies on the trajectory of $\mathbf{d}(k_y)$, rendering the winding number ill-defined.

The w in Eq. (9) is mathematically equivalent to the Zak phase γ_y . The latter can also serve as a topological invariant [82], which is equal to 0 (π) in the topologically trivial (nontrivial) phase of the SSH model. However, for the multi-band Hamiltonian $H_x(k_x)$ along x , the

Zak phases $\gamma_x = (\gamma_{12}, \gamma_{23})$ of the two band gaps are not enough to characterize all topological phases [50]. For instance, $\gamma_x = (0, \pi)$ indicates a pair of degenerate edge states between the second and third bands, $\gamma_x = (\pi, 0)$ leads to a pair of degenerate edge states between the first and second bands, $\gamma_x = (\pi, \pi)$ implies the existence of two pairs of edge states in both band gaps, and $\gamma_x = (0, 0)$ signifies the absence of edge states. Nevertheless, this characterization remains incomplete for $H_y(k_y)$, as edge states may still emerge even when $\gamma_{12} = \gamma_{23} = 0$ (see details in Appendix. A and Sec. III B). NATCs are then required to capture these additional topological features, offering a more complete description of multigap topological phases [41, 50].

The quasimomentum k_x is set along the azimuthal direction of the torus, forming a BZ as illustrated by the orange loop in Fig. 1(b). For each k_x loop, the eigenstates $\{|\psi(k_y)\rangle\}$ remain fixed, so that the topological properties are solely determined by the Hamiltonian $H_x(k_x)$ along x direction. Here, conventional Abelian topological invariants like the geometric phase are insufficient to characterize all distinct phases of $H(k_x)$. In this case, a matrix-valued, noncommutative topological invariant, namely the NATC, can be introduced [41]. For each eigenstate of our \mathcal{PT} -symmetric Hamiltonian $H_x(k_x)$, its three components $|\psi_p(k_x)\rangle = (\psi_{p1}(k_x), \psi_{p2}(k_x), \psi_{p3}(k_x))^T$ are real numbers, forming a three-dimensional (3D) eigenframe (x, y, z) . With the change of k_x , the eigenframe rotates in 3D Euclidean space [50]. The geometric features of the resulting NATCs are illustrated in Figs. 2(b)–(f), where the eigenstates $|\psi_{1,2,3}(k_x)\rangle$ are marked by red, green and blue dots for each k_x . As k_x goes from $-\pi$ to π , the size of the dots gradually increases. There are five distinct cases in total. (i) Two of the three vectors rotate by π around the third one [three distinct configurations in Figs. 2(b)–(d)], and the counter-rotations constitute their conjugate class; (ii) two of them rotate by 2π around the third [Fig. 2(e)]; and (iii) there are no rotations around any vectors [Fig. 2(f)]. For the latter two cases, the initial and final eigenframes are identical after the rotation. As a result, they cannot be distinguished by conventional geometric phases. However, they exhibit distinct properties: the former corresponds to a topological phase, while the latter represents a trivial one.

Under the given symmetry constraints, the eight geometric configurations above yield all possible topological structures of $H_x(k_x)$ with distinct NATCs, which are defined by the generalized Wilson loop

$$W = \hat{P} \exp \left[\oint_{-\pi}^{\pi} A(k_x) dk_x \right], \quad (10)$$

where \hat{P} is the path-ordering operator. The affine Berry-Wilczek-Zee (BWZ) connection $A(k_x)$ is given by

$$[A(k_x)]_{q,q'} = \langle \psi_q(k_x) | \partial_{k_x} | \psi_{q'}(k_x) \rangle. \quad (11)$$

The BWZ connection is antisymmetric and can be de-

composed by the generators of $\text{SO}(3)$, i.e., $A(k_x) = \sum_{p=1}^3 \beta_p L_p$ for $p = 1, 2, 3$. Using $\text{SU}(2)$ as a double cover of $\text{SO}(3)$, we can replace L_p by $t_p = -\frac{i}{2} \sigma_p$, yielding the affine BWZ connection $\bar{A}(k_x) = \sum_{p=1}^3 \beta_p t_p$. The NATC q_x accumulated along the BZ of k_x is then given by

$$q_x = \hat{P} \exp \left[\oint_{-\pi}^{\pi} \bar{A}(k_x) dk_x \right]. \quad (12)$$

The geometric structure of non-Abelian topological states has eight distinct classes, allowing the NATCs q_x to have eight matrix values from different rotations around the axes, i.e.,

$$q_x = \{\sigma_0, \pm i\sigma_x, \pm i\sigma_y, \pm i\sigma_z, -\sigma_0\}. \quad (13)$$

It is isomorphic to the quaternion group, given by

$$Q_x = \{1, \pm i, \pm j, \pm k, -1\}. \quad (14)$$

The $\pm\pi$ rotations around $x/y/z$ axes correspond to the charges $\pm i / \pm j / \pm k$. The $\pm 2\pi$ rotations around the $x/y/z$ axes correspond to the charge $(\pm i)^2 = (\pm j)^2 = (\pm k)^2 = -1$. The topological phases of $H_x(k_x)$ are therefore depicted by these NATCs. The elements $\pm i$, $\pm j$ and $\pm k$ belong to distinct conjugacy classes. The charge -1 corresponds to a topological phase that cannot be described by conventional geometric phases. In contrast, the trivial phase is characterized by the identity element 1. The NATCs i , j , k and 1 map onto the Zak phases $(0, \pi)$, (π, π) , $(\pi, 0)$ and $(0, 0)$, respectively. The NATC -1 cannot be described by Zak phases, highlighting the necessity of non-Abelian characterizations [41, 50].

B. Edge states of 1D subsystems

The Kronecker sum structure of 2D Hamiltonian H allows its eigensystem to be expressed as the sum and tensor product of eigenvalues and eigenstates of 1D Hamiltonians H_x and H_y along two directions ($E = E_x + E_y, |\Psi\rangle = |\Psi_x\rangle \otimes |\Psi_y\rangle$). Consequently, the topological properties of the 2D system can be deduced from those of the 1D subsystems. Here, we present their topological characteristics in order to clarify the non-Abelian origin of corner and edge states in our 2D model. The explicit forms of H_y and H_x are given in Eqs. (4) and (5). Their corresponding energy spectra are shown in Fig. 3(a) and Figs. 3(b)–(e).

The Hamiltonian $H_y(k_y)$ in Eq. (4) describes an SSH model. When $|J_1| < |J_2|$ the system enters a topologically nontrivial phase. It hosts a pair of degenerate edge modes at zero energy under OBC, characterized by a winding number $w = 1$ or a Zak phase $\gamma = \pi$ under PBC. When $|J_1| > |J_2|$ the system becomes topologically trivial and exhibits no edge states, corresponding to $w = 0$ or $\gamma = 0$. The topological phase transition occurs at $|J_2| = |J_1|$. The spectrum and IPR of H_y can be ob-

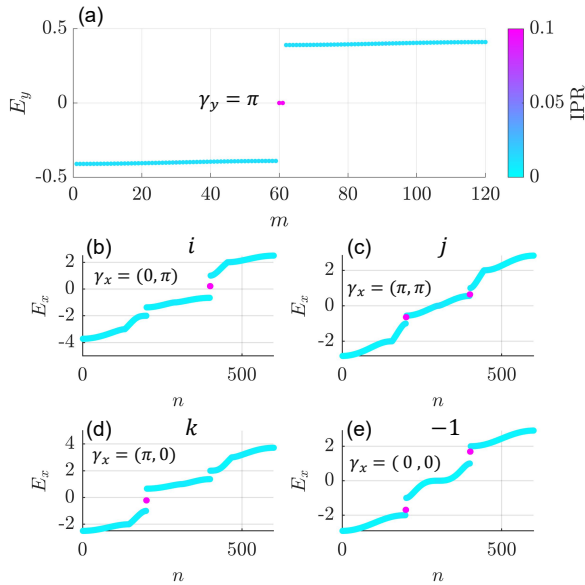


FIG. 3. Spectrum of 1D subsystems H_x and H_y . All panels share the same color bar, which indicates the magnitude of IPR for each state. (a) shows the spectrum of H_y in its topologically nontrivial region with $J_1 = 0.01$ and $J_2 = 2/5$. (b)–(e) show the spectrum and IPR of H_x . We set $\varphi = \pi$ for (b); $\varphi = 3\pi/2$ for (c); $\varphi = 0$ for (d); $\varphi = \pi/2$ For (e). Other parameters are set as $J_{AA} = -1$, $2J_{BB} = -u = v = 1$, and $S_A = S_B = 0$.

tained from the eigenvalue equation $H_y |\Psi_y\rangle = E_y |\Psi_y\rangle$ and $\text{IPR} = \sum_{m=1}^{L_y} |\langle m | \Psi_y \rangle|^4$. The resulting spectrum in the topologically nontrivial regime is illustrated in Fig. 3(a). It includes a pair of edge states (in pink color) at $E_y = 0$, which are protected by the chiral symmetry of H_x . All other states are bulk ones, whose IPR values tend to zero in the limit $L_y \rightarrow \infty$.

The Hamiltonian H_x along x -direction is given by Eq. (4), which satisfies $H_x |\Psi_x\rangle = E_x |\Psi_x\rangle$. We present the spectrum of H_x with NATCs $Q_x = i, j, k, -1$ under OBC in Figs. 3(b)–(e). The pink dots highlight edge states with large IPR. In Figs. 3(b) and 3(d), the upper and lower band gaps each holds two degenerate edge states. These cases correspond to the NATCs i and k . The Zak phase description remains valid for them, with the corresponding values $\gamma_x = (0, \pi)$ and $(\pi, 0)$. Two pairs of doubly degenerate edge states are observed in Fig. 3(c). Each of them is located in a different band gap, corresponding to the case with NATC j . Here, the Zak phase could also capture the existence of these edge states. In Fig. 3(e), although two pairs of doubly degenerate edge states emerge in the two gaps, they correspond to the NATC -1 . In this case, the Zak phase description breaks down, since both band gaps exhibit trivial Zak phases $\gamma_x = (0, 0)$ despite the presence of topological edge states. It demonstrates that the Zak phase is insufficient to classify non-Abelian topological phases and highlights the necessity of NATCs. Further details about

the anomalous edge states of phase -1 are shown in Appendix B. They can be regarded as phases generated by i^2 , j^2 , and k^2 , where the corresponding edge states appear in their respective band gaps, leading to the doubling of edge state numbers in Fig. 7.

In essence, the corner states of 2D system H originate from the hybridization of Abelian topology (the winding number of H_y) and non-Abelian topology (the NATC of H_x). This establishes our minimal model as a realization of non-Abelian SOTIs, whose phase structure will be revealed in the next subsection.

C. Hybridized invariant for higher-order topology

The above discussions have identified suitable topological invariants for our subsystem Hamiltonians. A system formed by their direct sum should carry the product topology of the quaternion charge and winding number of $H_x(k_x)$ and $H_y(k_y)$. The resulting topological invariant, as element of the $\text{SU}(2) \times \text{U}(1)$ group, takes the form

$$\nu = (Q_x, w) \in \mathbb{Q}_8 \times \mathbb{Z}, \quad (15)$$

where Q_x and w denote the NATC and winding number of $H_x(k_x)$ and $H_y(k_y)$. The multiplication rule between two such hybridized NATCs, as acquired by a direct product group $G = \mathbb{Q}_8 \times \mathbb{Z}$, is given by

$$\nu_1 \circ \nu_2 \equiv (Q_{x1} Q_{x2}, w_1 + w_2). \quad (16)$$

The winding number $w \in \mathbb{Z}$ is additive and obeys the commutative law $w_1 + w_2 = w_2 + w_1$. The additivity of Abelian topological invariants implies that the total topological charge can typically be obtained by summing the contributions from subsystems, or, in multiband systems, by accumulating the topological invariants of all occupied (valence) bands. Meanwhile, the quaternions are not commutative, e.g., $ij = -ji = k$. Therefore, the topological charge ν also does not satisfy the commutative law for any $Q_{x1}, Q_{x2} \in \{\pm i, \pm j, \pm k\}$. All possible values of ν thus form a non-Abelian group. In summary, the SOTIs in our 2D system H can be fully characterized by a hybridized NATC ν . Accordingly, four distinct configurations of topological charge could arise depending on the values of the two components of ν : (i) both w and Q_x are nontrivial, (ii) only the quaternion charge Q_x is nontrivial, (iii) only the winding number w is nontrivial, and (iv) both invariants are trivial.

For case (i), despite both topological charges being nontrivial, multiple distinguishable topological phases occur due to the quaternion charge Q_x . These phases are characterized by the hybridized invariant $\nu = (\pm i, 1)$, $(\pm j, 1)$, $(\pm k, 1)$ and $(-1, 1)$. A phase diagram containing all these phases is shown in Fig. 4. In case (ii), while the winding number w is trivial, the system hosts a family of first-order topological phases characterized by the nontrivial Q_x . They are weak topological phases with non-Abelian edge bands, which can also be identified in

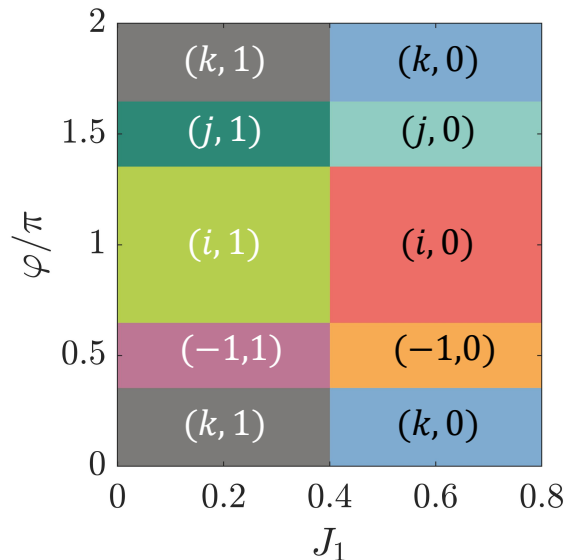


FIG. 4. Phase diagram of 2D non-Abelian HOTPs characterized by hybrid topological charge $\nu = (w, Q_x)$. Different SOTI phases are indicated by distinct colored regions, with their topological invariants shown therein. The system parameters are set as $S_C = 2 \cos \varphi$, $J_{CC} = \frac{1}{2} + \frac{1}{2} \sin \varphi$, $J_2 = \frac{2}{5}$, $J_{AA} = -1$, $2J_{BB} = -u = v = 1$, and $S_A = S_B = 0$.

Fig. 4. For case (iii), the quaternion charge becomes trivial while the winding number w is nontrivial. The topology is then governed by the 1D winding number, showing only Abelian edge bands. The cases (ii) and (iii) form a complementary pair, each capturing only one aspect of the hybridized invariant $\nu = (Q_x, w)$. Finally, both the winding number w and quaternion charge Q_x are trivial in case (iv), making the hybridized invariant $\nu = (1, 0)$. This regime represents a trivial insulating phase without any signatures of first- and second-order topology.

The emergence of corner and edge states under OBC depends on the interplay of invariants Q_x and w . Hybridized non-Abelian corner states appear exclusively in case (i), where both the w and Q_x are nontrivial. Case (ii) hosts weak non-Abelian edge bands when the OBC and PBC are taken along the x and y directions, while case (iii) exhibits weak Abelian edge bands when the OBC and PBC are taken along the y and x directions. Case (iv) supports no boundary states. A detailed analysis of these edge and corner states is given in Sec. IV.

The hybridized topological invariant ν is computed using Eqs. (9) and (12). In the resulting phase diagram Fig. 4, when $J_1 < 0.4$, the winding number $w = 1$ and the quaternion charge Q_x takes nontrivial values. In this regime, both $H_x(k_x)$ and $H_y(k_y)$ contribute nontrivial topology, endowing the full 2D model with a family of distinguishable non-Abelian HOTPs. These phases differ by the geometry of eigenstates $|\Psi_{p\pm}(\mathbf{k})\rangle$, where $|\psi_{\pm}(k_y)\rangle$ share the same winding number w but $|\psi_p(k_x)\rangle$ undergoes distinct rotations for different values of φ . As dis-

cussed in Sec. IV A, these differences are directly manifested in the energy distribution of corner states under OBC. When $J_1 > 0.4$, the winding number $w = 0$ and $H_y(k_y)$ becomes topological trivial. In this region, only weak non-Abelian topological edge bands survive under OBC (see Sec. IV B for details).

The non-Abelian HOTPs with charge $(-1, 1)$ can be realized through multiple mechanisms, and a representative case is presented in Fig. 4. In particular, different $(-1, 1)$ phases can be transformed into each other without closing and reopening the energy gap, indicating that they are topologically equivalent. The distinctions among their corner states are discussed in Appendix B.

To summarize, we have introduced a hybridized invariant $\nu = (Q_x, w)$, constructed from both Abelian and non-Abelian topological charges, to characterize 2D second-order topological phases of non-Abelian origins. Moreover, our minimal model supports both Abelian (with the Q_x component unchanged) and non-Abelian (with the w component unchanged) topological transitions via changing system parameters, bridging two seemingly incompatible topological classes into a unified framework. This unification not only enriches the landscape of HOTPs, but also yields more exotic bulk-boundary correspondences as will be discussed in the next section.

IV. BULK-EDGE-CORNER CORRESPONDENCE

In Sec. II B, we have performed a qualitative analysis on the topological edge and corner states of our 2D lattice model. In this section, we proceed to a more thorough discussion of these boundary modes and their relations to the hybrid non-Abelian topological invariants of the bulk. We first consider in Sec. IV A the corner states in cases where both H_x and H_y are set in topologically nontrivial regimes. Subsequently, we reveal weak topological edge bands arising from the coupling between topological edge states in one dimension and trivial bulk states in the other in Sec. IV B.

A. Non-Abelian topological corner states

The theory developed in the last section implies that non-Abelian corner states could appear in our 2D system described by H if and only if the quaternion charge and winding number of its 1D subsystems satisfy $Q_x \neq 1$ and $w \neq 0$. With the knowledge of edge states of H_x and H_y in mind, we could arrive at the following rules of bulk-corner correspondence for our minimal model, i.e.,

$$N_c = \begin{cases} 4|w||Q_x^2|, & Q_x = \pm i, \pm k, \\ 8|w||Q_x^2|, & Q_x = \pm j, -1, \\ 0, & Q_x = 1, \end{cases} \quad (17)$$

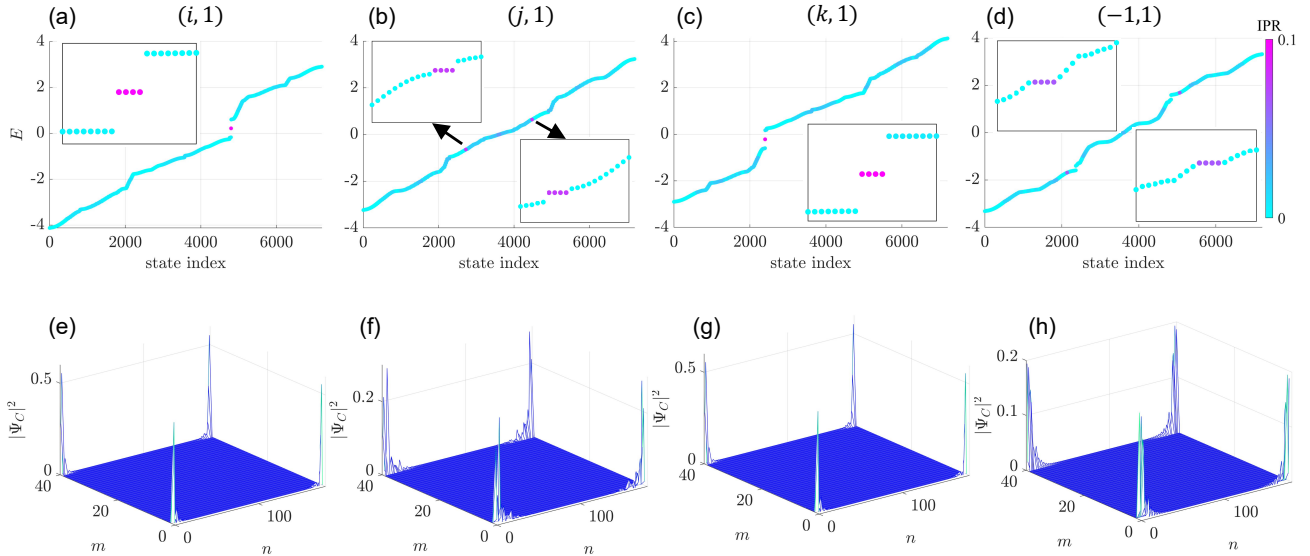


FIG. 5. Spectrum and corner states of the minimal non-Abelian HOTI model under OBC along both dimensions. (a)–(d) show the spectra of the system for different values of φ . The insets highlight the energy windows of corner states. The shared color bar indicates the IPR of each eigenstate. (e)–(h) show the probability distributions of corner states in the spectra (a)–(d). We set $J_1 = 0.01$, $J_2 = 0.4$, and $\varphi = \pi$ for (a), (e); $\varphi = 3\pi/2$ for (b), (f); $\varphi = 0$ for (c), (g); and $\varphi = \pi/2$ for (d), (h). Other parameters are equal to those of Fig. 4. The lattice size is $N = 60$ and $M = 40$.

where N_c denotes the total number of corner states for each given set of bulk topological charge $\nu = (Q_x, w)$.

The first equality in Eq. (17) states that we will find $N_c = 4|w|$ corner states on the Fermi surface of the 2D system at $2/3$ and $1/3$ fillings provided that $Q_x = \pm i$ and $\pm k$, respectively. In these two cases, the subsystem H_y owns two Abelian edge states $|\varphi_0^{(1)}\rangle$ and $|\varphi_0^{(2)}\rangle$ at zero energy for $w = 1$, while the subsystem H_x has two non-Abelian edge states $|\psi_E^{(1)}\rangle$ and $|\psi_E^{(2)}\rangle$ at the same energy $E \in \Delta_{23}$ ($E \in \Delta_{12}$) for $Q_x = \pm i$ ($Q_x = \pm k$), where Δ_{12} (Δ_{23}) denotes the spectral gap between the first and second (second and third) bulk bands of H_x . The hybridization of these edge states along two orthogonal dimensions results in four non-Abelian corner states $|\Psi_E^{(\ell, \ell')}\rangle = |\psi_E^{(\ell)}\rangle \otimes |\varphi_0^{(\ell')}\rangle$ at the same energy E of the 2D Hamiltonian $H = H_x \oplus H_y$, where $\ell, \ell' = 1, 2$. Their fourfold degeneracy is protected by the combined \mathcal{PT} and chiral symmetries of subsystems H_x and H_y .

The second equality in Eq. (17) states that we have $N_c = 4|w|$ corner states on the Fermi surface of the 2D system at both $1/3$ and $2/3$ fillings if $Q_x = \pm j$ or -1 . In these two cases, the subsystem H_y again has two Abelian edge states $|\varphi_0^{(1)}\rangle$ and $|\varphi_0^{(2)}\rangle$ at zero energy for $w = 1$. Meanwhile, the subsystem H_x has two non-Abelian edge states $|\psi_E^{(1)}\rangle$ and $|\psi_E^{(2)}\rangle$ at the energy $E \in \Delta_{12}$ and two other non-Abelian edge states $|\psi_{E'}^{(1)}\rangle$ and $|\psi_{E'}^{(2)}\rangle$ at the energy $E \in \Delta_{23}$. Their hybridization along two orthogonal dimensions leads to two groups of fourfold-degenerate non-Abelian corner states at the energies E and E' , given by $|\Psi_E^{(\ell, \ell')}\rangle = |\psi_E^{(\ell)}\rangle \otimes |\varphi_0^{(\ell')}\rangle$ and $|\Psi_{E'}^{(\ell, \ell')}\rangle = |\psi_{E'}^{(\ell)}\rangle \otimes |\varphi_0^{(\ell')}\rangle$ for $\ell, \ell' = 1, 2$. The degeneracy within each group of these

corner states is also protected by the combined \mathcal{PT} and chiral symmetries of subsystems H_x and H_y .

The third equality in Eq. (17) states that we have no corner states anywhere if $Q_x = 1$, regardless of the value of winding number w . In this case, the subsystem H_x does not support non-Abelian edge states. The edge zero modes of H_y , if exists, can only couple to the extended bulk states of H_x , yielding delocalized states in either the 2D bulk of the full system H or along its 1D edges.

The above analyses confirm that the number of corner states in each of our second-order topological phases is determined by the hybridized non-Abelian topological charge $\nu = (Q_x, w)$. Yet, as the edge states of subsystem H_y are pinned to zero energy, the energy spans of our corner states are controlled by the spectrum of edge states of subsystem H_x under OBC. As a remark, one may not be able to deduce whether the bulk charge is $(j, 1)$ or $(-1, 1)$ by directly viewing the spectrum of H under OBC, as the corner states look similar in these two cases. This issue might be resolved by comparing the following two situations. Let us assume that two distinct phases of Hamiltonian H , with bulk charges ν and $\nu' = (i, 1)$, are realized in two square lattices. The two systems are then coupled together at a single corner. If the invariant $\nu = (j, 1)$, the quotient rule of NATCs will induce a domain wall charge $\nu/\nu' = (j/i, 1) = (k, 1)$, yielding corner states at the coupled corner when the composite system H is set at $1/3$ filling. On the other hand, if $\nu = (-1, 1)$, the quotient rule of NATCs will induce a domain wall charge $\nu/\nu' = (-1/i, 1) = (i, 1)$, yielding corner states at the coupled corner when the composite system H is set at $2/3$ filling. The non-Abelian phases with bulk charges

$(j, 1)$ and $(-1, 1)$ can then be distinguished by investigating their domain-wall behaviors under OBC.

To illustrate the bulk-corner correspondence, we compute the spectra and corner states of our minimal model H for its typical non-Abelian second-order topological phases. The results are shown in Fig. 5. To distinguish the bulk states from corner states in the spectra, we evaluate the inverse participation ratio (IPR) for each 2D eigenstate of H in the lattice space, which is given by

$$\text{IPR}_q = \sum_{n=1}^N \sum_{m=1}^{M/2} \sum_{\alpha=A,B,C} |\langle n, m, \alpha | \Psi_q \rangle|^4. \quad (18)$$

Here, $|\Psi_q\rangle$ denotes the q th eigenstate of H . The total number of such states is $3MN$. If the $|\Psi_q\rangle$ represents an extended bulk state, we will have $\text{IPR}_q \rightarrow 0$ in the limits $N, M \rightarrow \infty$, and the numerical value of IPR_q would become vanishingly small when the total number of sites $N \times M$ is large enough. If the $|\Psi_q\rangle$ describes a localized corner state, we will obtain a finite IPR_q even in the limits $N, M \rightarrow \infty$, and the numerical value of IPR_q would be drastically different from zero for finite number of sites $N \times M$. Using the value of IPR_q as the color code of each eigenstate then allows us to discriminate bulk and corner states in the spectrum from their localization nature.

In Fig. 5(a), we observe four degenerate eigenmodes in the gapped energy regime $E \in \Delta_{23}$. They are indeed localized at the four corners of the 2D lattice, as reflected by their probability distributions in Fig. 5(e). For this example, the system parameters are taken in the region with topological charge $\nu = (i, 1)$ in Fig. 4. The hybridized non-Abelian bulk-corner correspondence, as described by the first equality in Eq. (17), is then verified. In Fig. 5(b), we observe four degenerate eigenmodes in each of the gapped energy regions $E \in \Delta_{12}$ and $E' \in \Delta_{23}$. These eight eigenstates are all localized at the corners of the 2D lattice, as shown in Fig. 5(f). In this case, the system parameters are chosen in the regime with topological charge $\nu = (j, 1)$ in Fig. 4. The bulk-corner correspondence, as described by the second equality in Eq. (17), is again verified. In Fig. 5(c), we find four degenerate eigenstates in the gapped energy regime $E \in \Delta_{12}$. They are located at the four corners of the 2D lattice, as presented in Fig. 5(g). Moreover, the system parameters for this example are chosen in the region with topological charge $\nu = (k, 1)$ in Fig. 4, thus confirming the bulk-corner correspondence in the first equality of Eq. (17). Finally, we identify four degenerate eigenstates in each of the energy regions $E \in \Delta_{12}$ and $E' \in \Delta_{23}$ in Fig. 5(d). Their spatial profiles are localized at the four corners of the 2D lattice in Fig. 5(h), although they are not energetically well separated from the bulk. In this case, the system parameters are chosen in the regime with topological charge $\nu = (-1, 1)$ in Fig. 4, verifying the bulk-corner correspondence in the second equality of Eq. (17). In summary, we have testified the bulk-corner correspondence in Eq. (17) for all typical phases of our 2D non-Abelian SOTIs. Com-

pared to Abelian SOTIs, the key difference is that due to the nontrivial quaternion component Q_x in the hybridized topological charge ν , each of the phases and its corner states here are of non-Abelian origin.

In more general situations, since the hybridized non-Abelian topological charge $(-1, 1) = (i^2, 1) = (j^2, 1) = (k^2, 1)$, 2D non-Abelian SOTIs may also possess corner modes exclusively in its spectral gaps Δ_{12} or Δ_{23} , yielding richer configurations of non-Abelian corner states. We discuss explicit examples for these cases in Appendix B. Besides, 1D edge bands of non-Abelian origin can arise in our system if the quaternion charge component Q_x of ν is nontrivial, as will be uncovered in the next subsection.

B. Non-Abelian topological edge bands

As mentioned in the last subsection, if any one the components of $\nu = (Q_x, w)$ is nontrivial, the edge states of its associated subsystem can bind to the bulk states of the rest subsystem, forming boundary states localized along a single direction at certain edges of the 2D lattice. Since the formation of these edge states depends on the type of boundary conditions, we refer to them as weak topological edge states and group them into two classes depending on which component of ν is nontrivial. Interestingly, these edge states could also be of non-Abelian origins when they are topological, as clarified below.

In the first class, the hybridized charge of the 2D system takes the form $\nu = (Q_x, 0)$ with $Q_x \neq 1$. In this case, the subsystem H_y hosts only trivial insulator phases. Taking the OBC and PBC separately along x and y directions, we can obtain a set of edge bands vs the conserved quasimomentum k_y of $H_y(k_y)$, as illustrated in Figs. 6(a)–6(c). For each state $|\Psi(k_y)\rangle$, the IPR there is defined as $\sum_{n=1}^N \sum_{\alpha=A,B,C} |\langle n, \alpha | \Psi(k_y) \rangle|^4$. The total number of these edge bands N_{ex} is determined by the quaternion charge Q_x . For our minimal model, the resulting bulk-edge correspondence reads

$$N_{ex} = \begin{cases} 4|Q_x^2|, & Q_x = \pm i, \pm k, \\ 8|Q_x^2|, & Q_x = \pm j, -1. \end{cases} \quad (19)$$

These relations are of non-Abelian origins due to the non-commutative nature of Q_x . We will be left with $N_{ex} = 0$ if $Q_x = 1$. The prefactors of $|Q_x^2|$ come from the fact that each non-Abelian edge state of H_x is twofold degenerate and $H_y(k_y)$ has two bulk bands at $\pm E_y(k_y)$. Therefore, if $Q_x = \pm i$ ($\pm k$), the two edge states $|\psi_E^{(1)}\rangle$ and $|\psi_E^{(2)}\rangle$ of H_x will couple to the Bloch states $|\varphi_{\pm}(k_y)\rangle$ of $H_y(k_y)$ with energies $\pm E_y(k_y)$ at each k_y , yielding two sets of twofold-degenerate edge bands $|\Psi_{E,\pm}^{(\ell)}(k_y)\rangle = |\psi_E^{(\ell)}\rangle \otimes |\varphi_{\pm}(k_y)\rangle$ with $\ell = 1, 2$ and $k_y \in [-\pi, \pi]$ at the energies $E \pm E_y(k_y)$, where the $E \in \Delta_{23}$ ($E \in \Delta_{12}$) for H_x . Meanwhile, if $Q_x = \pm j$ or -1 , the four edge states $|\psi_E^{(1)}\rangle, |\psi_E^{(2)}\rangle, |\psi_{E'}^{(1)}\rangle$ and $|\psi_{E'}^{(2)}\rangle$ of H_x will bind to the Bloch states $|\varphi_{\pm}(k_y)\rangle$

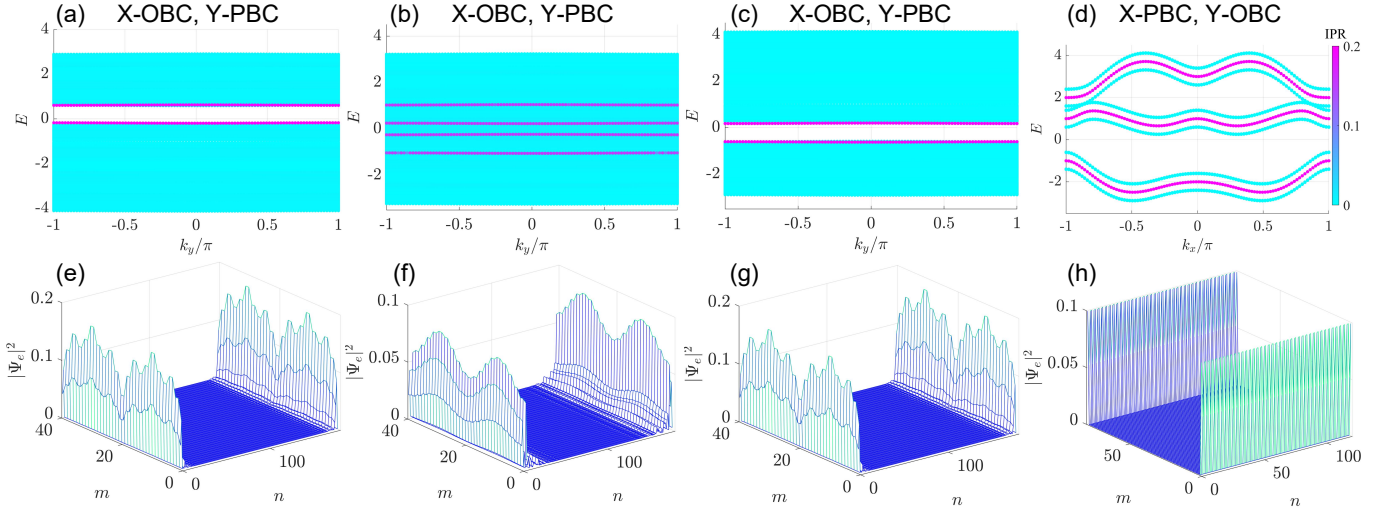


FIG. 6. Spectrum and edge states of the minimal non-Abelian HOTI model. (a)–(d) show the energy spectrum under MBC. For (a)–(c), we take the OBC (PBC) along the x (y) direction of the lattice. For (d), we take PBC (OBC) along the x (y) direction of the lattice. In (e)–(h), we plot edge states with the largest twenty IPRs in (a)–(d). System parameters used in (a)–(c) are identical to those in Figs. 5(a)–(c). (c) and (d) share the same parameters but have different boundary conditions.

of $H_y(k_y)$ with energies $\pm E_y(k_y)$ at each k_y , forming four sets of twofold-degenerate edge bands $|\Psi_{E,\pm}^{(\ell)}(k_y)\rangle = |\psi_E^{(\ell)}\rangle \otimes |\varphi_{\pm}(k_y)\rangle$ and $|\Psi_{E',\pm}^{(\ell)}(k_y)\rangle = |\psi_{E'}^{(\ell)}\rangle \otimes |\varphi_{\pm}(k_y)\rangle$ with $\ell = 1, 2$ and $k_y \in [-\pi, \pi)$ at the energies $E \pm E_y(k_y)$ and $E' \pm E_y(k_y)$, where the $E \in \Delta_{12}$ and $E' \in \Delta_{23}$ for H_x . As the topology of these edge bands are characterized by the quaternion charge Q_x , they constitute a unique type of non-Abelian weak topological edge states protected by the \mathcal{PT} symmetry of H_x , which implies that they could even be robust to perturbations that break the chiral symmetry of subsystem H_y . In this sense, we may regard this class of edge bands as sub-symmetry-protected non-Abelian topological states. In Figs. 6(e)–6(g), we show the edge states in Figs. 6(a)–6(c) under the OBC along both dimensions. The observed edge states are indeed localized only along x direction at the left and right boundaries of the 2D lattice.

In the second class, the hybridized charge of the 2D system reads $\nu = (Q_x, 1)$, so that the subsystem H_y hosts topological insulator phases with two edge zero modes under OBC. Taking the PBC and OBC separately along x and y directions, we obtain a set of edge bands vs the conserved quasimomentum k_x of $H_x(k_x)$, as illustrated in Fig. 6(d). There, the IPR is defined as $\sum_{m=1}^{M/2} |\langle m | \Psi(k_x) \rangle|^4$ for each state $|\Psi(k_x)\rangle$. For any Q_x , the total number of such edge bands is given by

$$N_{ey} = 6|w|, \quad Q_x \in \mathbb{Q}_8. \quad (20)$$

The prefactor “6” comes from the fact that the subsystem $H_x(k_x)$ holds three bulk bands $\{E_p(k_x) | p = 1, 2, 3\}$ with Bloch states $\{|\psi_p(k_x)\rangle | p = 1, 2, 3\}$ for $k_x \in [-\pi, \pi)$, regardless of its quaternion charge, and each edge state of H_y is twofold degenerate at zero energy. For our minimal

model with $w = 1$, the resulting six edge bands form three degenerate subsets with dispersion relation $E_p(k_x)$ and eigenstates $|\Psi_p^{(1)}(k_x)\rangle = |\psi_p(k_x)\rangle \otimes |\varphi_0^{(1)}\rangle$, $|\Psi_p^{(2)}(k_x)\rangle = |\psi_p(k_x)\rangle \otimes |\varphi_0^{(2)}\rangle$ for $p = 1, 2, 3$, where $|\varphi_0^{(1)}\rangle$ and $|\varphi_0^{(2)}\rangle$ are edge zero modes of H_y . In each subset, the degeneracy of edge bands is protected by the chiral symmetry of H_y , which is then robust to perturbations that break the \mathcal{PT} symmetry of subsystem $H_x(k_x)$. In this sense, we can regard this class of edge bands as sub-symmetry-protected topological states, which are formally of Abelian origins as their numbers are solely controlled by the winding number w . Nevertheless, when the \mathcal{PT} symmetry is preserved and the quaternion charge $Q_x \neq 1$, nontrivial eigenframe rotations could develop within the subspace of edge bands of $H(k_x) = H_x(k_x) \oplus H_y$, yielding weak topological edge states with non-Abelian characters as revealed by the nontrivial value of Q_x . The manipulation of these non-Abelian states at the edges may further lead to \mathcal{PT} -symmetry-protected braiding operations, which may find applications in future quantum technologies. Finally, we confirm in Fig. 6(h) that the edge states of our second class are indeed localized only along y direction at the top and bottom boundaries of the 2D lattice when OBC is taken along both dimensions.

In summary, both the edge and corner states of our system are characterized by the hybridized bulk topological charge $\nu = (Q_x, w)$. Non-Abelian second-order corner states arise if and only if both components of ν are nontrivial, and they coexist with first-order topological edge states of non-Abelian characters. If merely one component of ν is nontrivial, the system supports weak topological edge states of either non-Abelian (with $w = 0$) or Abelian (with $Q_x = 1$) origins, which are protected by the sub-symmetry of the rest nontrivial subsystem.

When both components of ν are trivial, the system becomes a trivial insulator, hosting neither edge nor corner topological states. We thus established a complete bulk-edge-corner correspondence for 2D non-Abelian HOTPs satisfying our coupled-wire construction.

V. CONCLUSION AND DISCUSSION

In this work, we introduced a theoretical framework to construct both intrinsic and hybridized non-Abelian HOTPs. Their underlying topology was found to be characterized by the tensor product of topological charges coming from distinct Abelian and non-Abelian groups of constituent subsystems. Focusing on the minimal model of non-Abelian HOTPs as an illustrative example, we revealed a rich set of non-Abelian SOTIs in experimentally realizable 2D lattices, which were protected by the united chiral and \mathcal{PT} symmetries. Each of the discovered phase was uniquely identified by a two-component change $\nu = (Q_x, w)$, with the Q_x and w be noncommutable quaternions and integers, respectively. A phase is then topological if and only if both two components of ν are nontrivial. Besides uncovering a series of non-Abelian second-order topological phases and phase transitions, we also found the correspondence between the bulk topological invariant ν , the configurations of corner states in rectangular geometries and of edge states in cylinder geometries for each of the non-Abelian SOTIs, thereby establishing a unified perspective on their bulk-edge-corner correspondences. Notably, we obtained 1D weak topological edge bands of non-Abelian origins, whose topologically-protected braiding may find applications in quantum information and computation related tasks. Overall, our work not only extends the study of HOTPs to non-Abelian domains, but also blends the Abelian and non-Abelian topological phases into a single context, opening avenues for more systematic classifications of their topological nature.

In experiments, transmission line networks have been proven to be efficient for simulating high-dimensional lattice models and probing their physical properties. For example, three dimensional waveguide networks have been employed to observe Anderson localization [83], while two dimensional honeycomb networks have been used to emulate Chern insulators [84]. More importantly, this platform has been applied to the realization of non-Abelian first-order topological phases by connecting nodes through waveguides [50, 51]. One can then construct quasi-1D lattice models with long-range hoppings, where each sublattice site within a unit cell serves as a node and the intercell couplings are implemented as long-range connections. When all nodes are connected by cables of equal length and each node is attached to the same number of cables, the wave equation at each node in the lossless limit becomes equivalent to the Schrödinger equation of a tight-binding model. In this situation, with all cables having identical lengths, different coupling

strengths are implemented by varying the number of connections between nodes. Onsite potentials can be realized by adding self-connected cables to the nodes. Under these conditions, a transmission line network provides a flexible means to simulate our lattice models. Measuring the voltage at each node corresponds to probing the wave amplitude. By injecting a signal at one end and measuring the resulting global voltage distribution, one can directly obtain the spatial profile of the wave function. These advances provide strong experimental support for the feasibility of realizing our model in transmission line networks. Therefore, we expect the full topological features of our model, including the non-Abelian corner and edge states, to be observable in such setups under current experimental capabilities.

In future work, since our coupled-wire scheme is generic, it can be used to construct intrinsic non-Abelian SOTIs in two dimensions and other non-Abelian HOTPs in higher dimensions, whose topological charges are still obtainable following our theoretical framework. Beyond equilibrium, unique non-Abelian HOTPs may arise in non-Hermitian and Floquet systems, whose topological properties are still awaited to be revealed. Finally, the robustness of non-Abelian HOTPs to disorder and interactions would be important for their practical applications, which thus deserve more thorough explorations.

ACKNOWLEDGMENTS

This work is supported by the National Natural Science Foundation of China (Grants No. 12275260 and No. 11905211), the Fundamental Research Funds for the Central Universities (Grant No. 202364008), and the Young Talents Project of Ocean University of China.

Appendix A: Zak phase

In this Appendix, we analyze the topological properties of our system from the perspective of Abelian geometric phase. We reveal that this approach becomes insufficient for depicting non-Abelian HOTPs [41, 50].

In 1D systems, the Zak phase [85] offers a geometric indicator of topological states. A quantized Zak phase $\gamma = \pi \pmod{2\pi}$ typically signals a nontrivial phase that supports degenerate edge states, whereas $\gamma = 0$ corresponds to a topologically trivial insulating phase. For an isolated band, the Zak phase is given by the integral of Berry connection $A(k)$ over the Brillouin zone, i.e.,

$$\gamma = \oint_{\text{BZ}} A(k) dk = i \oint_{\text{BZ}} \langle u_k | \partial_k | u_k \rangle dk, \quad (\text{A1})$$

where $|u_k\rangle$ denotes the Bloch eigenstate. Therefore, the Zak phase corresponds to the geometric Berry phase accumulated by a Bloch state during an adiabatic traversal of the Brillouin zone.

For SSH model, the Zak phase serves as a topological invariant equivalent to the winding number, which could faithfully characterize the bulk-edge correspondence. For our 1D Hamiltonian $H_y(k_y)$, the Berry connection of its valence band is given by

$$A(k_y) = i \langle \psi_-(k_y) | \partial_{k_y} | \psi_-(k_y) \rangle, \quad (\text{A2})$$

where $|\psi_-(k_y)\rangle$ denotes the eigenstate of lower band, yielding the Zak phase following Eq. (A1). In the main text, Fig. 3(a) shows the spectrum of SSH model as our subsystem H_x . Using Eqs. (A1) and (A2), we find the corresponding Zak phase in Fig. 3(a). When H_y lies in a topological phase, the Zak phase $\gamma_y = \pi$, and a pair of edge states arise in the spectrum at $E_y = 0$. When $\gamma_y = 0$, there are no edge states and the system becomes topologically trivial.

However, the Zak phase is no longer a reliable topological invariant for our subsystem H_x . To see this, let us try to use the Zak phase of occupied bands as an indicator of edge states within each gap. For the lower gap, we focus on the Zak phase $\gamma_{12} = \gamma_1$ of the first band of $H_x(k_x)$. For the upper gap, we use the sum of Zak phases of the first and second bands, given by $\gamma_{23} = \gamma_1 + \gamma_2$. For our three-band Hamiltonian $H_x(k_x)$, we have $\gamma_x \equiv (\gamma_{12}, \gamma_{23})$, and the Zak phase of each band reads

$$\gamma_p = i \oint \langle \psi_p(k_x) | \partial_{k_x} | \psi_p(k_x) \rangle dk_x, \quad p = 1, 2, 3, \quad (\text{A3})$$

where $|\psi_p(k_x)\rangle$ is the p th eigenvector of $H_x(k_x)$. In Figs. 3(b)–3(e), we show the energy spectra and IPR of H_x under OBC, with the Zak phases labeled in each panel. For NATCs $Q_x = i, j, k, 1$, the Zak phase correctly reflects the topology of each band gap. For example, in Fig. 3(b), a pair of edge states appears in the upper band gap, corresponding to $\gamma_x = (0, \pi)$ and NATC i . In Fig. 3(d), two pairs of edge states arise in both gaps, corresponding to $\gamma_x = (\pi, \pi)$ and NATC j . In Fig. 3(e), a pair of edge states appears in the lower band gap, corresponding to $\gamma_x = (\pi, 0)$ and NATC k . For NATC -1 , we find two pairs of edge states under OBC. However, the Zak phase is $\gamma_x = (0, 0)$ in this case, identical to the trivial phase $Q_x = 1$ without edge states. This contradiction shows that the Zak phase fails to capture all phases of our model, making the introduction of NATCs essential. From another viewpoint, the eigenframe rotations of H_x show at least five distinct patterns [Figs. 2(b)–2(e)]. However, a system with two band gaps allows at most $2^2 = 4$ combinations of Zak phases. This discrepancy demonstrates that the Zak phase cannot capture the overall non-Abelian topology encoded in H_x .

Appendix B: Non-Abelian SOTIs with charge $(-1, 1)$

In Sec. IV A, we examined the corner states arising in various topological phases of Fig. 4. In this Appendix, we focus on a particular phase with charge $\nu = (-1, 1)$ and

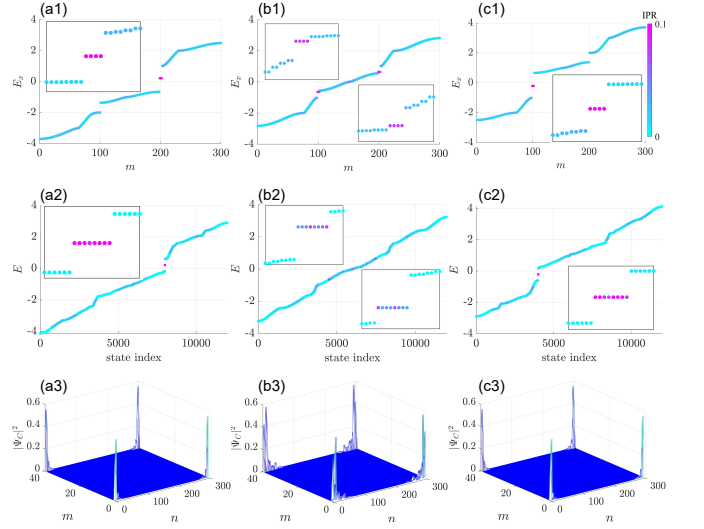


FIG. 7. Spectra and IPR of non-Abelian SOTIs under OBC. (a1)–(c1) show energy spectra of the Hamiltonian H' . They share the NATC $Q_x = -1$. (a2)–(c2) show energy spectra of the 2D Hamiltonian \mathcal{H} . (a3)–(c3) show probability distributions of the corner states in (a2)–(c2). The insets highlight the edge and corner states. (a1)–(c1) and (a2)–(c2) have the same color bar, which represents the magnitude of IPR. In (a)–(c), the NNN hopping amplitudes are the same as the NN hopping amplitudes in Figs. 5(a)–(c), i.e., $J'_{\alpha\alpha'} = J_{\alpha\alpha'}$.

analyze its distinctive features in detail. As discussed in Sec. III, the topological phase of H_x with $Q_x = -1$ has no analogs in geometric phase descriptions. Under OBC, this phase further reveals enriched edge state configurations, which distinguishes it from both Abelian and other non-Abelian topological phases. Due to the quaternion relations $i^2 = j^2 = k^2 = -1$, the $Q_x = -1$ case may be realized by doubled eigenframe rotations of the charge i, j or k . Although these quaternion elements are equivalent and can be continuously deformed into one another [50], they exhibit distinct edge state structures under OBC.

To further reveal the peculiarity of the $(-1, 1)$ phase, we introduce next-nearest-neighbor (NNN) hoppings along the x -direction in the model shown in Fig. 1. The NNN Hamiltonian in momentum space reads

$$H'_x(k_x) = \begin{pmatrix} V'_{AA} & 2u' \sin 2k_x & 0 \\ 2u' \sin 2k_x & V'_{BB} & 2v' \sin 2k_x \\ 0 & 2v' \sin 2k_x & V'_{CC} \end{pmatrix}, \quad (\text{B1})$$

where $V'_{\alpha\alpha} \equiv S_\alpha + 2J'_{\alpha\alpha} \cos 2k_x$ for $\alpha = A, B, C$. The spectra of $H'_x(k_x)$ under OBC are shown in Figs. 7(a1)–7(c1). Although sharing the same NATC $Q_x = -1$, these cases exhibit different edge-mode distributions. This discrepancy comes from different physical effects associated with i^2, j^2 and j^2 . In particular, the spectrum in Fig. 7(a1) hosts a single set of fourfold degenerate edge states in the upper band gap, whereas the spectrum in Fig. 7(b1) contains two such sets, each residing in a different band gap. Thus, even though i^2 and j^2 are equivalent

representatives of $Q_x = -1$, the physical arrangements of edge states retains clear signatures of their distinctive eigenframe-rotation axes. Note in passing that all phases with $Q_x = -1$ has a trivial Zak phase $\gamma_x = (0, 0)$.

The 1D non-Abelian phase $Q_x = -1$ in different quaternion representatives shows distinct edge state configurations under OBC, yielding different degeneracies and spectral locations for corner states in the 2D system. With NNN hoppings, the 2D model has the Hamiltonian $\mathcal{H}(\mathbf{k}) = H'_x(k_x) \otimes \sigma_0 + \mathbb{I}_3 \otimes H_y(k_y)$. Its spectra, corresponding to the same hybridized charge $\nu = (-1, 1)$, are shown in Figs. 7(a2)–7(c2). In each case, the corner modes arise from the interplay between topological edge states contributed by H'_x and H_y . In Figs. 7(a2) and 7(c2), there is a set of corner states with eightfold degeneracy. Their energy corresponds to those of edge states Figs. 7(a1) and 7(c1). In Fig. 7(b2), there are two sets of eightfold degenerate corner states.

Their energies are consistent with those of edge states in Fig. 7(b1). The probability distributions of localized states in Figs. 7(a2)–7(c2) are shown in Figs. 7(a3)–7(c3), respectively, which are indeed pinned to the system corners. Here, the key feature of the non-Abelian SOTI phase with charge $\nu = (-1, 1)$ is that while the bulk invariant determines the overall topological class, the corner states can display distinct configurations. That is, although the $Q_x = -1$ charge generated by different eigenframe rotations are topologically equivalent in the bulk, they leave distinct signatures in the energy spectra under OBC. These corner state distributions can be smoothly transformed into one another. Essentially, the eigenenergies of our corner state are governed by the quaternion component Q_x , while the winding number w leads to an additional twofold degeneracy for each corner state, yielding the final configuration of hybridized non-Abelian corner states in our system.

-
- [1] M. Z. Hasan and C. L. Kane, Colloquium: topological insulators, *Rev. Mod. Phys.* **82**, 3045 (2010).
- [2] X.-L. Qi and S.-C. Zhang, Topological insulators and superconductors, *Rev. Mod. Phys.* **83**, 1057 (2011).
- [3] C.-K. Chiu, J. C. Y. Teo, A. P. Schnyder, and S. Ryu, Classification of topological quantum matter with symmetries, *Rev. Mod. Phys.* **88**, 035005 (2016).
- [4] X.-G. Wen, Colloquium: Zoo of quantum-topological phases of matter, *Rev. Mod. Phys.* **89**, 041004 (2017).
- [5] M. Sato and Y. Ando, Topological superconductors: a review, *Rep. Prog. Phys.* **80**, 076501 (2017).
- [6] S. Rachel, Interacting topological insulators: a review, *Rep. Prog. Phys.* **81**, 116501 (2018).
- [7] X. Zhang, F. Zangeneh-Nejad, Z.-G. Chen, M.-H. Lu, and J. Christensen, A second wave of topological phenomena in photonics and acoustics, *Nature* **618**, 687 (2023).
- [8] X. Chen, Essay: Generalized landau paradigm for quantum phases and phase transitions, *Phys. Rev. Lett.* **135**, 250001 (2025).
- [9] K. v. Klitzing, G. Dorda, and M. Pepper, New method for high-accuracy determination of the fine-structure constant based on quantized hall resistance, *Phys. Rev. Lett.* **45**, 494 (1980).
- [10] D. J. Thouless, M. Kohmoto, M. P. Nightingale, and M. den Nijs, Quantized hall conductance in a two-dimensional periodic potential, *Phys. Rev. Lett.* **49**, 405 (1982).
- [11] F. D. M. Haldane, Model for a quantum hall effect without landau levels: Condensed matter realization of the "parity anomaly", *Phys. Rev. Lett.* **61**, 2015 (1988).
- [12] X.-L. Qi, Y.-S. Wu, and S.-C. Zhang, Topological quantization of the spin hall effect in two dimensional paramagnetic semiconductors, *Phys. Rev. B* **74**, 085308 (2006).
- [13] C.-Z. Chang, J. Zhang, X. Feng, J. Shen, Z. Zhang, M. Guo, K. Li, Y. Ou, P. Wei, L.-L. Wang, *et al.*, Experimental observation of the quantum anomalous hall effect in a magnetic topological insulator, *Science* **340**, 167 (2013).
- [14] C. L. Kane and E. J. Mele, Quantum spin hall effect in graphene, *Phys. Rev. Lett.* **95**, 226801 (2005).
- [15] C. L. Kane and E. J. Mele, z_2 topological order and the quantum spin hall effect, *Phys. Rev. Lett.* **95**, 146802 (2005).
- [16] B. A. Bernevig, T. L. Hughes, and S.-C. Zhang, Quantum spin hall effect and topological phase transition in hgte quantum wells, *Science* **314**, 1757 (2006).
- [17] M. König, S. Wiedmann, C. Brune, A. Roth, H. Buhmann, L. W. Molenkamp, X.-L. Qi, and S.-C. Zhang, Quantum spin hall insulator state in hgte quantum wells, *Science* **318**, 766 (2007).
- [18] B. Yan and S.-C. Zhang, Topological materials, *Rep. Prog. Phys.* **75**, 096501 (2012).
- [19] Y. Ren, Z. Qiao, and Q. Niu, Topological phases in two-dimensional materials: a review, *Rep. Prog. Phys.* **79**, 066501 (2016).
- [20] B. J. Wieder, B. Bradlyn, J. Cano, Z. Wang, M. G. Vergniory, L. Elcoro, A. A. Soluyanov, C. Felser, T. Neupert, N. Regnault, and B. A. Bernevig, Topological materials discovery from crystal symmetry, *Nat. Rev. Mater.* **7**, 196 (2022).
- [21] Y. Ashida, Z. Gong, and M. Ueda, Non-hermitian physics, *Adv. Phys.* **69**, 249 (2020).
- [22] E. J. Bergholtz, J. C. Budich, and F. K. Kunst, Exceptional topology of non-hermitian systems, *Rev. Mod. Phys.* **93**, 015005 (2021).
- [23] N. Okuma and M. Sato, Non-hermitian topological phenomena: A review, *Annu. Rev. Condens. Matter Phys.* **14**, 83 (2023).
- [24] R. Lin, T. Tai, L. Li, and C. H. Lee, Topological non-hermitian skin effect, *Frontiers of Physics* **18**, 53605 (2023).
- [25] A. Banerjee, R. Sarkar, S. Dey, and A. Narayan, Non-hermitian topological phases: principles and prospects, *J. Phys.: Condens. Matter* **35**, 333001 (2023).
- [26] T. Oka and S. Kitamura, Floquet engineering of quantum materials, *Annu. Rev. Condens. Matter Phys.* **10**, 387 (2019).
- [27] M. S. Rudner and N. H. Lindner, Band structure engineering and non-equilibrium dynamics in floquet topological insulators, *Nat. Rev. Phys.* **2**, 229 (2020).

- [28] F. Harper, R. Roy, M. S. Rudner, and S. Sondhi, Topology and broken symmetry in floquet systems, *Annu. Rev. Condens. Matter Phys.* **11**, 345 (2020).
- [29] S. Bandyopadhyay, S. Bhattacharjee, and D. Sen, Driven quantum many-body systems and out-of-equilibrium topology, *J. Phys.: Condens. Matter* **33**, 393001 (2021).
- [30] L. Zhou and D.-J. Zhang, Non-hermitian floquet topological matter—a review, *Entropy* **25**, 1401 (2023).
- [31] S. Ryu, A. P. Schnyder, A. Furusaki, and A. W. W. Ludwig, Topological insulators and superconductors: tenfold way and dimensional hierarchy, *New J. Phys.* **12**, 065010 (2010).
- [32] Z. Gong, Y. Ashida, K. Kawabata, K. Takasan, S. Higashikawa, and M. Ueda, Topological phases of non-hermitian systems, *Phys. Rev. X* **8**, 031079 (2018).
- [33] K. Kawabata, K. Shiozaki, M. Ueda, and M. Sato, Symmetry and topology in non-hermitian physics, *Phys. Rev. X* **9**, 041015 (2019).
- [34] S. Lieu, M. McGinley, and N. R. Cooper, Tenfold way for quadratic lindbladians, *Phys. Rev. Lett.* **124**, 040401 (2020).
- [35] R. Roy and F. Harper, Periodic table for floquet topological insulators, *Phys. Rev. B* **96**, 155118 (2017).
- [36] C.-H. Liu, H. Hu, and S. Chen, Symmetry and topological classification of floquet non-hermitian systems, *Phys. Rev. B* **105**, 214305 (2022).
- [37] X. Liu, A. B. Culver, F. Harper, and R. Roy, Classification of unitary operators by local generatability, *Phys. Rev. B* **111**, 085149 (2025).
- [38] M. Kléman, L. Michel, and G. Toulouse, Classification of topologically stable defects in ordered media, *J. Phys. (Paris), Lett.* **38**, 195 (1977).
- [39] N. D. Mermin, The topological theory of defects in ordered media, *Rev. Mod. Phys.* **51**, 591 (1979).
- [40] L. A. Madsen, T. J. Dingemans, M. Nakata, and E. T. Samulski, Thermotropic biaxial nematic liquid crystals, *Phys. Rev. Lett.* **92**, 145505 (2004).
- [41] Q. Wu, A. A. Soluyanov, and T. Bzdušek, Non-abelian band topology in noninteracting metals, *Science* **365**, 1273 (2019).
- [42] A. Bouhon, Q. Wu, R.-J. Slager, H. Weng, O. V. Yazyev, and T. Bzdušek, Non-abelian reciprocal braiding of weyl points and its manifestation in zrte, *Nat. Phys.* **16**, 1137 (2020).
- [43] F. N. Ünal, A. Bouhon, and R.-J. Slager, Topological euler class as a dynamical observable in optical lattices, *Phys. Rev. Lett.* **125**, 053601 (2020).
- [44] B. Jiang, A. Bouhon, Z.-K. Lin, X. Zhou, B. Hou, F. Li, R.-J. Slager, and J.-H. Jiang, Experimental observation of non-abelian topological acoustic semimetals and their phase transitions, *Nat. Phys.* **17**, 1239 (2021).
- [45] B. Peng, A. Bouhon, B. Monserrat, and R.-J. Slager, Phonons as a platform for non-abelian braiding and its manifestation in layered silicates, *Nat. Commun.* **13**, 423 (2022).
- [46] W. Zhao, Y.-B. Yang, Y. Jiang, Z. Mao, W. Guo, L. Qiu, G. Wang, L. Yao, L. He, Z. Zhou, *et al.*, Quantum simulation for topological euler insulators, *Commun. Phys.* **5**, 223 (2022).
- [47] B. Peng, A. Bouhon, R.-J. Slager, and B. Monserrat, Multigap topology and non-abelian braiding of phonons from first principles, *Phys. Rev. B* **105**, 085115 (2022).
- [48] S. Kwon and B.-J. Yang, Quantum geometric bound and ideal condition for euler band topology, *Phys. Rev. B* **109**, L161111 (2024).
- [49] M. Finck, D. Solnyshkov, J. Dubois, and G. Malpuech, Dirac points annihilation and its obstruction characterized by euler number and quaternionic charges in kagome lattice, *arXiv preprint arXiv:2507.19238* (2025).
- [50] Q. Guo, T. Jiang, R.-Y. Zhang, L. Zhang, Z.-Q. Zhang, B. Yang, S. Zhang, and C. T. Chan, Experimental observation of non-abelian topological charges and edge states, *Nature* **594**, 195 (2021).
- [51] T. Jiang, Q. Guo, R.-Y. Zhang, Z.-Q. Zhang, B. Yang, and C. T. Chan, Four-band non-abelian topological insulator and its experimental realization, *Nat. Commun.* **12**, 6471 (2021).
- [52] D. Wang, Y. Wu, Z. Zhang, and C. Chan, Non-abelian frame charge flow in photonic media, *Phys. Rev. X* **13**, 021024 (2023).
- [53] Y. Liu, Y. Li, J. Chen, X. Wang, H. Zhang, F. Guan, and X. Jiang, Two types of non-abelian topological phase transitions under duality mapping in 1d photonic chains, *Adv. Sci.* **2025**, e11935 (2025).
- [54] X.-C. Sun, J.-B. Wang, C. He, and Y.-F. Chen, Non-abelian topological phases and their quotient relations in acoustic systems, *Phys. Rev. Lett.* **132**, 216602 (2024).
- [55] Z.-X. Chen, Y.-H. Zhang, X.-C. Sun, R.-Y. Zhang, J.-S. Tang, X. Yang, X.-F. Zhu, and Y.-Q. Lu, Direct measurement of topological invariants through temporal adiabatic evolution of bulk states in the synthetic brillouin zone, *Phys. Rev. Lett.* **134**, 136601 (2025).
- [56] Q.-D. Wang, Y.-Q. Zhu, S.-L. Zhu, and Z. Zheng, Synthetic non-abelian topological charges in ultracold atomic gases, *Phys. Rev. A* **110**, 023321 (2024).
- [57] Y. Yang, B. Yang, G. Ma, J. Li, S. Zhang, and C. Chan, Non-abelian physics in light and sound, *Science* **383**, eadf9621 (2024).
- [58] T. Jiang, R.-Y. Zhang, Q. Guo, B. Yang, and C. Chan, Two-dimensional non-abelian topological insulators and the corresponding edge/corner states from an eigenvector frame rotation perspective, *Phys. Rev. B* **106**, 235428 (2022).
- [59] Y. Zhou, C. Li, X. Wang, and X. Zhou, Waveguiding in two-dimensional floquet non-abelian topological insulators, *arXiv preprint arXiv:2508.12678* (2025).
- [60] Y. Qi, Z. He, J. Li, B. Yan, Z. Zhang, and K. Deng, Experimental realization of non-abelian higher-order topological insulators in two-dimensional phononic crystals, *Phys. Rev. B* **111**, 134113 (2025).
- [61] T. Li and H. Hu, Floquet non-abelian topological insulator and multifold bulk-edge correspondence, *Nat. Commun.* **14**, 6418 (2023).
- [62] H. Qiu, S. Tong, Q. Zhang, K. Zhang, and C. Qiu, Observation of anomalous floquet non-abelian topological insulators, *arXiv preprint arXiv:2508.06818* (2025).
- [63] Q. Lin, T. Li, H. Hu, W. Yi, and P. Xue, Simulating floquet non-abelian topological insulator with photonic quantum walks, *arXiv preprint arXiv:2508.06466* (2025).
- [64] Y. Liang, R. Wang, Z. Yu, J. Chen, L. Xiao, S. Jia, and L. Zhang, Three-band non-hermitian non-abelian topological insulator with pt symmetry, *Phys. Rev. B* **109**, 115127 (2024).
- [65] W. A. Benalcazar, B. A. Bernevig, and T. L. Hughes, Quantized electric multipole insulators, *Science* **357**, 61 (2017).
- [66] J. Langbehn, Y. Peng, L. Trifunovic, F. Von Oppen, and P. W. Brouwer, Reflection-symmetric second-order topo-

- logical insulators and superconductors, Phys. Rev. Lett. **119**, 246401 (2017).
- [67] Z. Song, Z. Fang, and C. Fang, (d-2)-dimensional edge states of rotation symmetry protected topological states, Phys. Rev. Lett. **119**, 246402 (2017).
- [68] E. Khalaf, Higher-order topological insulators and superconductors protected by inversion symmetry, Phys. Rev. B **97**, 205136 (2018).
- [69] M. Geier, L. Trifunovic, M. Hoskam, and P. W. Brouwer, Second-order topological insulators and superconductors with an order-two crystalline symmetry, Phys. Rev. B **97**, 205135 (2018).
- [70] L. Li, M. Umer, and J. Gong, Direct prediction of corner state configurations from edge winding numbers in two- and three-dimensional chiral-symmetric lattice systems, Phys. Rev. B **98**, 205422 (2018).
- [71] W. A. Benalcazar and A. Cerjan, Chiral-symmetric higher-order topological phases of matter, Phys. Rev. Lett. **128**, 127601 (2022).
- [72] R. Okugawa, S. Hayashi, and T. Nakanishi, Second-order topological phases protected by chiral symmetry, Phys. Rev. B **100**, 235302 (2019).
- [73] R. W. Bomantara, L. Zhou, J. Pan, and J. Gong, Coupled-wire construction of static and floquet second-order topological insulators, Phys. Rev. B **99**, 045441 (2019).
- [74] F. Schindler, A. M. Cook, M. G. Vergniory, Z. Wang, S. S. Parkin, B. A. Bernevig, and T. Neupert, Higher-order topological insulators, Sci. Adv. **4**, eaat0346 (2018).
- [75] B. Xie, H.-X. Wang, X. Zhang, P. Zhan, J.-H. Jiang, M. Lu, and Y. Chen, Higher-order band topology, Nat. Rev. Phys. **3**, 520 (2021).
- [76] M. Kim, Z. Jacob, and J. Rho, Recent advances in 2d, 3d and higher-order topological photonics, Light Sci. Appl. **9**, 130 (2020).
- [77] W. Zhu, W. Deng, Y. Liu, J. Lu, H.-X. Wang, Z.-K. Lin, X. Huang, J.-H. Jiang, and Z. Liu, Topological phononic metamaterials, Rep. Prog. Phys. **86**, 106501 (2023).
- [78] J. Pan and L. Zhou, Non-hermitian floquet second order topological insulators in periodically quenched lattices, Phys. Rev. B **102**, 094305 (2020).
- [79] L. Zhou, Floquet second-order topological phases in momentum space, Nanomaterials **11**, 1170 (2021).
- [80] L. Zhou, Generating many majorana corner modes and multiple phase transitions in floquet second-order topological superconductors, Symmetry **14**, 2546 (2022).
- [81] L. Zhou, R. Wang, and J. Pan, Gapless higher-order topology and corner states in floquet systems, Phys. Rev. Res. **7**, 023079 (2025).
- [82] J. K. Asbóth, L. Oroszlány, and A. Pályi, *A short course on topological insulators*, Vol. 919 (Springer, 2016).
- [83] Z. Zhang, C. Wong, K. Fung, Y. Ho, W. Chan, S. Kan, T. Chan, and N. Cheung, Observation of localized electromagnetic waves in three-dimensional networks of waveguides, Phys. Rev. Lett. **81**, 5540 (1998).
- [84] T. Jiang, M. Xiao, W.-J. Chen, L. Yang, Y. Fang, W. Y. Tam, and C. Chan, Experimental demonstration of angular momentum-dependent topological transport using a transmission line network, Nat. Commun. **10**, 434 (2019).
- [85] J. Zak, Berry's phase for energy bands in solids, Phys. Rev. Lett. **62**, 2747 (1989).